Journal of Solid State Chemistry 184 (2011) 1001–1007

Contents lists available at ScienceDirect

Journal of Solid State Chemistry

journal homepage: www.elsevier.com/locate/jssc

Transparent oxyfluoride glass ceramics co-doped with Er^{3+} and Yb^{3+} – Crystallization and upconversion spectroscopy

I. Gugov [a,*], M. Müller [b], C. Rüssel [b]

[a] Department of Physics, University of Chemical Technology and Metallurgy, Sofia 1756, Bulgaria
[b] Otto-Schott-Institut, Jena, University, Germany

ARTICLE INFO

Article history:
Received 3 January 2011
Received in revised form
1 March 2011
Accepted 5 March 2011
Available online 15 March 2011

Keywords:
Nanocrystals
Growth kinetics
YbF_3
ErF_3
Anti-stokes luminescence

ABSTRACT

Transparent glass ceramics in the system SiO_2–B_2O_3–PbO–CdO–PbF_2–CdF_2–YbF_3–ErF_3 showing infrared to visible anti-Stokes (upconversion) luminescence are studied in the present work. The glass compositions have been optimized in order to reduce the melting temperature and, hence, to obtain laboratory scale samples with good optical quality. Erbium-doped nanoscale $Pb_4Yb_3F_{17}$ crystals are precipitated in the precursor glasses during annealing at temperatures 30–40 K above T_g. A kinetically self-constrained growth explains the nano sizes of the crystals. Both the Stokes and anti-Stokes luminescence spectra of glasses could be explained with clustering of the Yb^{3+} and Er^{3+} ions in fluorine-rich regions. At the annealing temperature these regions act as nucleation precursors. The crystal growth further enhances the local concentration of these ions. Consequently, a series of energy transfer and energy cross relaxation processes occurs between adjacent rare earth ions leading to the observed luminescence spectra of the glass ceramics studied.

1. Introduction

The ability of some rare-earth doped materials to transform efficiently near-infrared radiation into visible and ultraviolet light, NIR to VIS/UV upconversion, is of great interest due to the possible laser, amplifier, IR imaging, and luminescent bioassays applications. In that way, NIR laser diodes can be used as energy efficient and biologically inactive sources for VIS/UV operation. Auzel [1], one of the pioneering researchers in this field, published a comprehensive review with about 300 references considering history, fundamentals, and prospects of the upconversion materials.

Transparent oxyfluoride nanoglass-ceramics (NGC) containing PbF_2 and LnF_3 (Ln=rare earth ion(s)), are among the most promising and most frequently studied upconversion materials. Below we will denote these materials as PbF_2-NGC. Different glass formers such as SiO_2, GeO_2, SiO_2–GeO_2 and B_2O_3 have been used as matrices for this type of NGC [1–7].

The preparation of a PbF_2-NGC involves two steps: (i) an oxyfluoride glass is melted using standard techniques and (ii) the precursor glass is heat treated to form a PbF_2:LnF_3 nanophase. The size of the precipitated nanocrystals and, consequently, the optical transparency of the glass-ceramics are tailored by the variation of annealing time and temperature [1–7]. The rare-earth ions in these glasses are acting as nucleating agents [5], and are concentrated preferably in the fluoride nanocrystals [2,8]. As a result, the rare-earth ions attain an ordered, low phonon environment that enhances the intensity of upconversion luminescence by about two orders of magnitude in comparison with the non-crystallized glasses [2]. The glass matrix provides the mechanical and chemical stability of the resulting material.

The main drawback, concerning the known PbF_2-NGC is their relatively high melting temperature in connection with the high volatility of a part of the ingredients during the course of the melt process. Hence, reproducible preparation of luminescent materials with good optical quality is still a problem and new solutions should be preferred.

In the present work, we are reporting some new low melting and stable SiO_2–B_2O_3 based transparent PbF_2-NGC. Special attention is paid to the crystallization of the glasses as well as to the luminescence mechanisms in the glasses and the NGC. The crystallization and luminescence data are discussed together in order to build structural models that are consistent with the observed luminescence behavior.

2. Experimental

Conventional melting techniques were used to prepare the oxyfluoride glasses from reagent grade precursors with 3–5 N purity. The batches, calculated for 100 g glass, have been thoroughly mixed in closed plastic containers and then melted in a

* Corresponding author. Fax: +359 2 8685 488.
E-mail address: i.gugov@uctm.edu (I. Gugov).

0022-4596/$ - see front matter © 2011 Elsevier Inc. All rights reserved.
doi:10.1016/j.jssc.2011.03.017

covered platinum crucible in a SiC-rod furnace. In order to reduce the evaporation, mainly of SiF_4 and BF_3, the melting temperature was kept as a rule below 1200 K. During the melting time of 1–2 h, the melts were homogenized several times by stirring. The melts were poured into brass molds, preheated at temperatures 10 K below the glass transition temperature, T_g (typically about 650 K), and then cooled down within about 12 h. The obtained glasses have good chemical stability and mechanical workability. Most of them are transparent and appear as macroscopically homogeneous. The glasses were cut into pieces with dimensions $10\times10\times2$ mm^3 and annealed for 0.5–31 h at 660–720 K in order to obtain transparent nano glass-ceramics. Finally, the surfaces of the samples were ground and polished with optical quality.

Uncovered platinum and alumina crucibles were used for differential thermal analysis (DTA) and thermogravimetry (TG) under ambient atmosphere. The powdered samples were heated at the rate of 10 K/min.

Standard colorimetric technique was applied for the wet chemical analyses.

The X-ray diffraction (XRD) was performed on powdered as well as on bulk samples using Cu$K\alpha_1$(+Cu$K\alpha_2$) radiation ($\lambda=0.15406+0.15445$ nm) with a Siemens D 5000 diffractometer (SIEMENS AG, Karlsruhe, Germany) equipped with a SolX energy-dispersive detector. A corundum X-ray diffraction instrument response standard (NIST #1976a) was used to adjust thoroughly the diffractometer with respect to peak positions and intensities and to estimate the device specific values for the so-called fundamental parameter method. Cell parameters, crystal size and micro-strain were calculated from the X-ray patterns using the TOPAS 3 software (Bruker-AXS, Karlsruhe, Germany) for full pattern decomposition by the Pawley method and the Rietveld algorithm. First, only space group information was used for the calculation of cell parameters and crystal size, followed by a more detailed calculation based on the positions of the particular atoms in the (modified: Er replaced by Yb) unit cell for $Pb_{0.55}Er_{0.45}F_{2.45}$ given in [13]. Only five peaks were used for these calculations, the error in the cell parameters is about 1 pm.

A SHIMADZU UV-3101PC (SHIMADZU Corp., Kyoto, Japan) double beam spectrophotometer was used to measure the optical spectra of glasses and transparent glass-ceramics in the UV/VIS/NIR region (190–3200 nm). The sample thickness was 1 mm; the surfaces were polished to optical quality.

As pump source for the upconversion luminescence, an NIR laser diode emitting in cw operation mode at 940 nm was used. The pump power applied was about 0.5 W. The spectra were taken in 90° geometry using optical fibers for incident and output beams, without any additional lenses. The spectra were recorded using a 30 cm single beam grating monochromator with a CCD optical sensor. In the present work, the raw spectra (without correction for the spectral sensitivity of the equipment) are shown.

The density of bulk samples was measured at 293 K using a helium-gas picnometer.

3. Results and discussion

3.1. Preparation of the glass-ceramics

3.1.1. Glass preparation

First, the glass composition A as shown in Table 1 was used. Melting this composition for 30 min at 1173 K resulted in an opaque glass-ceramic sample. Increasing the melting temperature to 1323 K kept for 30 min improved the transparency, but a pale opalescence was still evident. In the later case, the thermogravimetry showed a substantial weight loss (around 10%) during melting. The weight loss measured by TG, is significant at any temperature above 973 K and increases notably at temperatures above 1250 K.

Table 1
Composition by synthesis of the glasses in mol%.

Composition	A[a]	B	C	D	E
SiO_2	21.8	21.0	21.0	20.0	20.0
Al_2O_3	5.2	7.0	7.0	7.0	7.0
B_2O_3	9.7	9.0	9.0	9.0	9.0
PbF_2	28.4	20.0	20.0	20.0	17.0
CdF_2	24.0	20.0	20.0	20.0	18.0
YbF_3	10.3	9.0	10.0	12.0	15.0
ErF_3	0.6	0.5	0.5	0.2	0.1
PbO		6.0	6.0	3.0	5.0
CdO		5.0	6.5	6.8	6.9
ZnO		2.0		2.0	2.0
$Al(PO_3)_4$		0.5			
Density (g/cm^3)	6.33	6.06	6.06	5.99	6.02

[a] Opaque

The fluoride constituents of glass A have boiling points at ambient pressure between 1563 K (PbF_2) and 2473 K (YbF_3) which is above the used melting temperatures. Therefore, some chemical interactions, taking place during melting, should be responsible for the immense weight losses. In our glass melts, such interactions are presumed to be:

$$CdF_2+H_2O\rightarrow CdO+2HF\uparrow \quad (1)$$

$$2CdF_2+SiO_2\rightarrow 2CdO+SiF_4\uparrow \quad (2)$$

$$3CdF_2+B_2O_3\rightarrow 3CdO+2BF_3\uparrow \quad (3)$$

Wet chemical analyses of glass A melted for 30 min at 1323 K showed, that the SiO_2 concentration decreases notably from 8.4 in the batch to 4.0 mass% in the glass. By analogy, B_2O_3 decreased from 4.3 to 2.9 mass% and fluorine from 16.5 to 9.0 mass%. The mass of all other glass constituents remained unchanged within the experimental error. Taking into account the atomic weights of the respective elements, it can be calculated that 7.6 mass% from the total weight loss of about 10 mass% results from the evaporation of SiF_4 (Eq. (2)), and 1.4 mass%—from the evaporation of BF_3 (Eq. (3)). The residual weight loss of 0.8 mass% is possibly assigned to dehydrogenation (Eq. (1)).

Eqs. (1)–(3) are a simplified illustration of the real processes, taking place during melting. In fact, at the supplied melting temperatures all ions are continuously changing their places and neighbors. Therefore, the first coordination sphere of a given cation is dynamic and contains both oxygen and fluorine anions in different proportions. If all first neighbor(s) of a hydrogen, silicon or boron ion, placed in vicinity of the melt surface became fluorine, the formed HF, SiF_4 or BF_3 molecules evaporate, reducing the fluorine and silicon, boron or proton content in melt. Eqs. (1)–(3) imply that the residual oxygen coordinates preferably the Cd^{2+} ions, while the Pb^{2+}, Er^{3+}, and Yb^{3+} ions remain predominately coordinated with fluorine. By means of extended X-ray absorption fine structure (EXAFS) measurements, Silva et al. observed a similar type of anion redistribution in some PbF_2–CdF_2–B_2O_3 glasses [7].

The high fluoride volatility at temperatures above 1250 K has two disadvantageous consequences: (i) it makes it difficult to control the final glass composition and the resulting materials' properties; (ii) it decreases the homogeneity of the respective glasses because of the continuous refractive index changes near the melt surface. For oxyfluoride melts as large as 1000 cm^3 and higher, this drawback could be overcome using advanced

facilities. The solution we choose for our laboratory scale (15 cm^3) melting technique was to develop compositions suitable to be melted below 1200 K. The compositions (synthesis) of a part of the prepared glasses are listed in Table 1. All glasses shown there, excluding glass A, have been melted for 60–120 min at several temperature steps between 1073 and 1173 K. They were kept for 30 min at the maximum temperature. At these preparation conditions, the glasses B–E were X-ray amorphous and visually transparent and homogeneous. The measured weight losses of about 3% are still notable, but reproducible and, at this point, satisfying for our research purposes. As it is evident from Table 1, stable glasses are obtained if PbF_2 and CdF_2 are partially replaced by PbO and CdO, respectively. Small quantities of ZnO are also helpful. The presence of B_2O_3 contributes to the reduction of the melting temperature. Consequently, it was possible to prepare clear glasses with 9–15 mol% YbF_3 (glasses B–E).

3.1.2. Crystallization of glasses

Fig. 1 presents DTA profiles of the glass C (upper curve) and a sample annealed at 703 K for 31 h (lower curve) of the same composition. Glass C has a glass transition temperature of 656 K, shows a large exothermic (crystallization) peak at 770 K and another very small one at about 870 K as well as two endothermic (melting) peaks at 1035 and 1103 K.

After annealing at 703 K for 31 h the peak at 770 K nearly disappeared and T_g increases up to the annealing temperature (703 K) (see in Fig. 1, bottom curve). This type of thermal evolution is an indication for a kinetically self-constrained nano-crystallization process, taking place in glass [9].

Fig. 2 shows the XRD patterns of glass C annealed at 703 K for different periods of time. The XRD patterns of the annealed

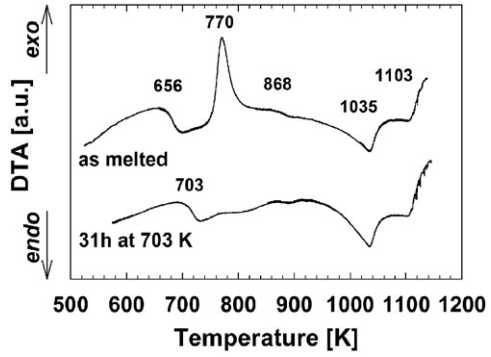

Fig. 1. DTA-profiles of glass C (upper curve) and of glass C annealed at 703 K for 31 h (lower curve).

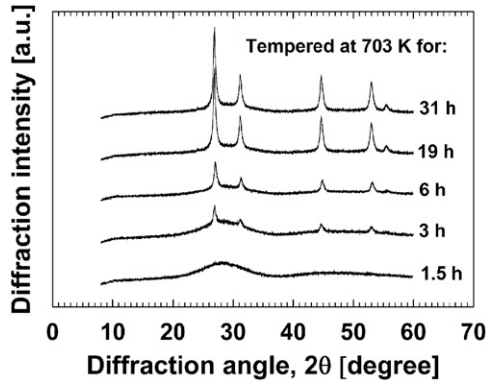

Fig. 2. XRD patterns of glass C annealed at a temperature of 703 K for 1.5, 3, 6, 19 and 31 h.

glasses B, D, and E are similar. The as-melted glasses as well as the sample annealed for 1.5 h (bottom curve in Fig. 2) are X-ray amorphous. The glasses annealed for longer periods of time show XRD peaks which at a first glance are attributable to a cubic fluorite-type structure with a lattice parameter, $a = 575 \pm 1$ pm.

The initial assumption made by Wang and Ohwaki [2] and of other authors [3,4,10] was that a fluorite-type solid solution ($Pb_xCd_{1-x}F_2$:*Ln*) crystallizes in NGC containing PbF_2 and CdF_2. However, by means of high resolution transmission electron microscopy (HRTEM) with energy-dispersive X-ray analysis (EDS), Kukkonen et al. [8] have demonstrated that the corresponding nanocrystals contain Pb^{2+}, Ln^{3+}, and F^-, but not Cd^{2+} ions. Moreover, they detected that the concentration of Ln^{3+} (Er^{3+}) ions in the crystalline phase is higher than in the precursor glass. The authors suggested that the crystalline phase is 'mainly PbF_2' and has lattice parameter, $a = 575$ pm [8]. Haas et al. [11] used anomalous small angle X-ray scattering (ASAXS) and also concluded on the occurrence of a $(Pb_{0.5}Yb_{0.5})F_{2.5}$ phase doped with erbium which does not contain any cadmium.

The absence of Cd^{2+} ions in the crystallized fluoride phase appears as a surprise if only the nominal glass compositions (in some cases up to 29 mol% CdF_2 [3]) are considered. On the contrary, this deficiency seems more natural if Cd^{2+} is presumed to be coordinated by oxygen or by oxygen and fluorine, as shown above. Thus, only the predominantly fluorine coordinated Pb^{2+} and Ln^{3+} ions segregate to form the new PbF_2:LnF_3 phase.

The phase diagrams of the PbF_2–LnF_3 systems [12,13] show large domains of solid solutions $Pb_{1-x}Ln_xF_{2+x}$, $0 < x \leq x_L$. The upper solid solution limit, x_L, depends on the type of Ln^{3+} (ionic radius) and on temperature. This limit is: $x_L = 0.30$ for Nd, $x_L = 0.25$ for Eu, and $x_L = 0.15$ for Er [13]. In the similar system PbF_2–YF_3 the limit is $x_L = 0.13$ at 823 K and $x_L = 0.20$ at 973 K [14]. The solid solutions have a cubic CaF_2-type structure with Pb^{2+} and Ln^{3+} ions statistically distributed over the cation positions. In principle, fluorine anions in interstitial sites may compensate the extra charge introduced through Ln^{3+} ions (see e.g. Ref. [13] and references therein) or, however, Pb^{2+} vacancies occur.

The lattice parameter, $a(x)$, of the solid solutions depends linearly on the composition [12–16]. Based on literature data, Fig. 3 illustrates this dependence.

Also shown in Fig. 3 are the pseudo-cubic lattice constants, a_{pcub}, calculated for the phases $Pb_{1-x}Ln_xF_{2+x}$, found in part of the PbF_2–LnF_3 systems. These phases have an ordered, fluorite-related

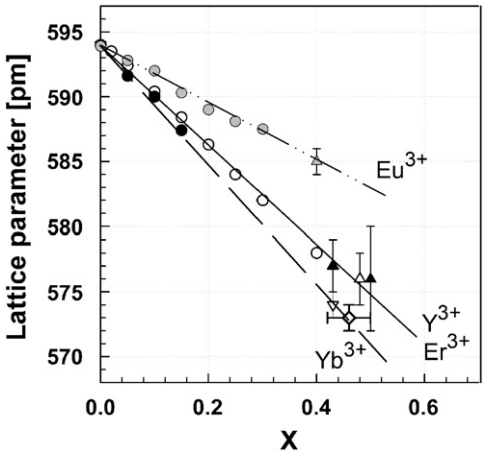

Fig. 3. Lattice parameter of the cubic $(1-x)PbF_2$–x LnF_3 solid solutions as a function of *x*. *Ln*: Er^{3+}—black circles, Y^{3+}—open circles, and Eu^{3+}—gray circles. The calculated pseudo-cubic lattice constants of the respective ordered phases (see text) are presented by open (Y) and black (Er) triangles. The open diamond presents the measured lattice constant and the estimated composition of the ordered phase precipitating in our glasses.

Table 2
Lattice parameters of some ordered phases with composition $Pb_{1-x}Ln_xF_{2+x}$ taken from the literature and the corresponding pseudo-cubic lattice constants, a_{pcub}, calculated using Eqs. (4)–(7).

Ln^{3+}	x	Structure	a (pm)	c (pm)	References	a_{pcub} (pm)
Eu^{3+}	0.40	Rhombohedral	1092.8	2027.8	[13]	585 ± 1
Y^{3+}	0.43	Rhombohedral	1081.4	1993.1	[14]	577 ± 2
Y^{3+}	0.48	Tetragonal	407.6	1740.0	[14]	576 ± 2
Er^{3+}	0.40	Rhombohedral	1080.4	1996.2	[13]	577 ± 2
Er^{3+}	0.50	Tetragonal	404.6	1738.6	[13]	576 ± 4
Yb^{3+}	0.43	Rhombohedral	1074.6	1985.4	[12]	574 ± 1

structure. The structures of phases $Pb_3Eu_2F_{12}$ [13], $Pb_4Y_3F_{17}$ [14], $Pb_4Er_3F_{17}$ [13] and $Pb_4Yb_3F_{17}$ [12] have rhombohedral distortion, while the structures of $Pb_{0.52}Y_{0.48}F_{2.48}$ and $PbErF_5$ [14] phases have tetragonal distortion. Peak splitting in XRD patterns illustrates this distortion. The appearance of some minor additional peaks suggests the presence of super-cells with respective symmetry [14]. The lattice constants of that type of phases are collected in Table 2. Two pseudo-cubic lattice constants are calculated for each phase using the formulae [14]:

$$a_{pcub,a} = \frac{2a_R}{\sqrt{14}} \tag{4}$$

and

$$a_{pcub,c} = \frac{c_R}{\sqrt{12}} \tag{5}$$

for the $Pb_4Ln_3F_{17}$ ($x=0.43$) phases with rhombohedral structure and superstructure (hexagonal settings), as well as

$$a_{pcub,a} = \frac{2a_T}{\sqrt{2}} \tag{6}$$

and

$$a_{pcub,c} = \frac{c_T}{3} \tag{7}$$

for the $Pb_{0.52}Ln_{0.48}F_{2.48}$ ($x=0.48$) phases with tetragonal structure and superstructure. The lattice parameters, a_{pcub}, shown in Table 2, are calculated as a median between $a_{pcub,a}$ and $a_{pcub,c}$. The difference between $a_{pcub,a}$ and $a_{pcub,c}$ is used to estimate the confidence interval for a_{pcub}.

As shown in Fig. 3 the straight lines $a(x)$ drawn for the solid solutions pass, within the uncertainty of estimation, through the lattice parameter a_{pcub} of the respective ordered phase. Since the composition is decisive for the respective structure and the lattice constant of the PbF_2:LnF_3 crystals, the straight lines in Fig. 3 enable to estimate the composition of the nanocrystals.

In our case, the lattice constant ($a=575 \pm 1$ pm) corresponds according to Fig. 3 (Yb and Er are related bottom lines) to $x=0.42 \pm 0.02$. The theoretical value calculated from the nominal composition of glass C (Table 1) is $x=0.33$. The larger concentration of rare earths ions in the nanocrystals has already been reported earlier by other authors [8]. It is possibly connected with the better ability of lanthanide ions to coordinate fluorine and to segregate into fluorine-rich regions in comparison to lead ions. This presumption is consistent also with the function of Ln^{3+} ions as nucleation agents in the PbF_2-NGC. As reported by Haas et al. ASAX measurements of a similar composition show a crystal composition of $(Pb_{0.5}Yb_{0.5})F_{2.5}$ for a glass with the ratio Pb/Yb=2.75, This confirms an enrichment of the fluoride crystals with the rare earth element [11].

The estimated value $x=0.42 \pm 0.02$ is well above the upper solid solution limit, $x_L=0.15$, in the system PbF_2–ErF_3 [13]. This suggests that ordered phases in spite of solid solutions crystallize in the NGC studied. This is plausible, despite the expected peak splitting and minor supplementary peaks are actually not observed in the experimental XRD patterns. According Beggiora et al. [16] in NGC these splittings and small supplementary peaks might be hidden by line broadening and scattering from the amorphous matrix. In our glasses the Erbium concentration is relatively low (see Table 1). In the PbF_2–YbF_3 system, however, only the rhombohedral phase $Pb_{0.57}Yb_{0.43}F_{2.43}$ ($Pb_4Yb_3F_{17}$) exists [12]. Therefore, we suppose that this phase, doped with some amount of Er^{3+} ions, crystallizes in glasses. Currently, we perform additional studies to verify this hypothesis.

From the peak broadening of the XRD patterns shown in Fig. 2, we estimated the mean size of the nanocrystals, using the Scherrer formula:

$$D(t) = \frac{C\lambda}{B(t)\cos(\theta)} \tag{8}$$

where $C=0.89$ for cubic shaped crystals, λ is the X-ray wavelength, $B(t)$ is the peak full width at half maximum (FWHM) corrected to the instrumental peak broadening, and θ is the diffraction angle (the reflection at $2\theta \approx 44.7^\circ$ is used in our case).

The experimental $D(t)$ data shown in Fig. 4 are fitted (solid line) by

$$D(t) = D_{max}\left[1-\exp\left(-\frac{t}{\tau}\right)\right] \tag{9}$$

Here, fit parameters are the maximum crystal size $D_{max} \cong 39$ nm and the time constant $\tau \cong 2.6$ h. This fit presumes a steady state nucleation, although we observed a time lag of about 1.5 h (see Fig. 2). This apparent time lag, however, might be related to the sensitivity threshold of the XRD method used.

The mean crystal growth velocity $U(t)$ is given by

$$U(t) = \frac{D_{max}}{2\tau}\exp\left(-\frac{t}{\tau}\right) \equiv U_0\exp\left(-\frac{t}{\tau}\right) \tag{10}$$

The crystal growth starts with a rate of $U_0=7$ nm/h and is practically zero after about 15 h. This type of crystallization kinetics as well as the observed evolution of the thermal properties of the glass matrix is consistent with the model of kinetically self-constrained growth, developed recently by Rüssel [9,17–25]. This model considers the devitrification of multi-component glasses when the T_g of residual glass matrix rises due to the depletion in those components, which form the crystallizing phase. A highly viscous shell, acting as diffusion barrier, is build in this case around the growing crystal. The effect of this barrier rises enormously if the shell's T_g approaches the annealing temperature. At that point, the crystal growth is fully suppressed for kinetic reasons despite a driving force for crystallization still exists [9,17–25]. The increase in viscosity has already been shown in systems from which Fe_3O_4 [17], CaF_2 [9] and [18], BaF_2 [9] and [21], or ß-quartz [22], have been crystallized. The occurrence

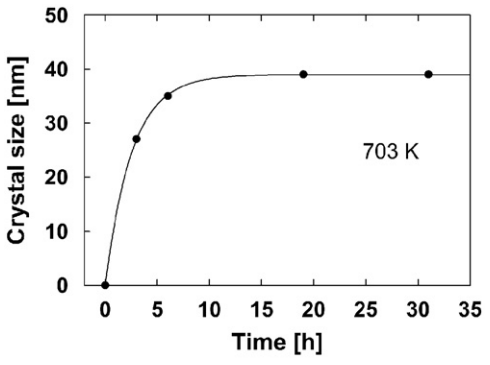

Fig. 4. The crystal size as calculated from XRD-line broadening using Scherrer equation as a function of time.

of core/shell structures has recently been proved by transmission electron microscopy [22,23]. These structures were recently also explained by theoretical models and numerical simulations [24,25].

3.2. Optical absorption and luminescence

3.2.1. Optical absorption

The optical absorption spectrum of glass C is shown in Fig. 5. The spectrum of the nano glass-ceramics obtained by annealing glass C at 693 K for 32 h (not shown) is similar to the spectrum in Fig. 5. The only differences are enhanced optical losses in the short wavelength region due to the slightly enhanced light scattering in the NGC. The observed peaks correspond to the ground state absorption (GSA) to different Er^{3+} energy levels and are partially labeled in Fig. 5. The peak positions are similar to those reported in the literature [26]. There are some slight discrepancies only for the $^4F_{9/2}$ line which peaks at 652 nm in glass C (657.8 nm in [26]) as well as for the telecommunication $^4I_{13/2}$ band positioned at 1529 nm in our glass (1512 nm in [26]). The strong absorption band in the 900–1000 nm range (see inset in Fig. 5) is mainly due to GSA of the Yb^{3+} ion. The absorption spectra of glasses and NGC A, B, D and E are similar to that of glass C.

3.2.2. Stokes luminescence

The Stokes luminescence spectra of glass B as melted (solid curve) and that of the sample annealed at 693 K for 5 h (dashed line) are shown in Fig. 6. The excitation at 375 nm was in the region of the $^4G_{11/2}$ absorption line. Surprisingly, the green luminescence from the $^4S_{3/2}$ level, typical for an Er^{3+} doped glass, is very weak. The red luminescence from the $^4F_{9/2}$ level is completely absent in the glass but appears in the spectrum of NGC (see Fig. 6).

The weakness of the green Stokes luminescence is possibly due to the low-phonon environment of Er^{3+} ions in both the glass and the NGC. The phonon energy in PbF_2-NGC was reported to be as low as 250 cm^{-1} [27]. Therefore, the nonradiative decay $^4G_{11/2} \rightarrow {}^2H_{9/2} \rightarrow {}^4F_{5/2}$ is hindered and the energy relaxation mainly occurs due to direct emission from the excited $^4G_{11/2}$ state. The weakness of the green Stokes luminescence may be also a result of concentration quenching due to a cross relaxation process $^2H_{11/2} + {}^4I_{15/2} \rightarrow {}^4I_{9/2} + {}^4I_{13/2}$ between adjacent Er^{3+} ions [28]. This process, however, should be operative in the anti-Stokes luminescence too leading to reduction of the green and red luminescence and enhancement of the $^4I_{9/2} \rightarrow {}^4I_{15/2}$ luminescence at about 800 nm. As it is evident from Fig. 10, this is not the case in the glass-ceramics B.

The appearance of $^4F_{9/2}$ luminescence in the NGC could be related to a resonant back energy transfer (BET) process $^4G_{11/2}$ (Er)+$^2F_{7/2}$ (Yb)→$^4F_{9/2}$ (Er)+$^2F_{5/2}$ (Yb) (Fig. 7), triggered from the increased concentration of the rare-earth (RE) ions in the NGC. A similar back energy transfer from Er^{3+} to Yb^{3+} ions, $^4F_{7/2}$ (Er)+$^2F_{7/2}$ (Yb)→$^4I_{11/2}$ (Er)+$^2F_{5/2}$ (Yb), is revealed in [29].

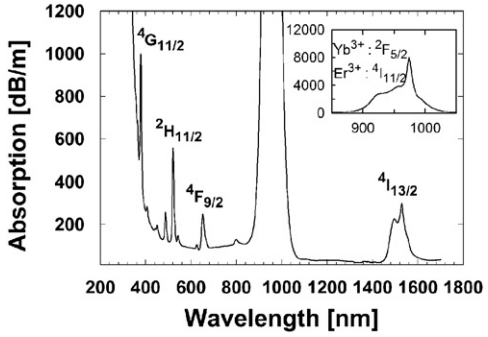

Fig. 5. Optical absorption spectrum of glass C. The spectra of other glasses and glass ceramics studied are similar.

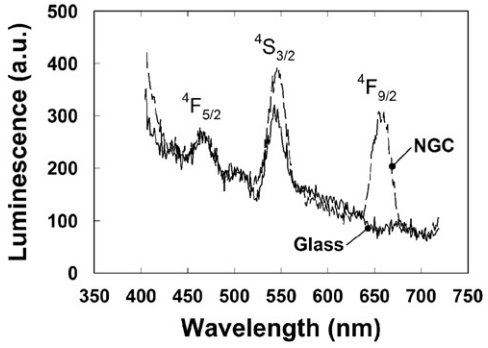

Fig. 6. Luminescence spectra of glass B (solid line) and of glass B subsequently annealed at 693 K for 5 h (dashed line).

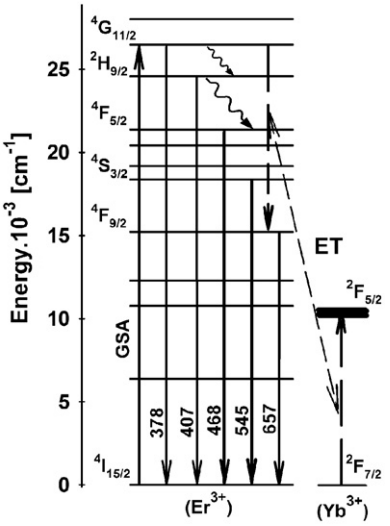

Fig. 7. Shematic diagram of the Er^{3+} luminescence after excitation in the $^4G_{11/2}$ absorption band. The assumed BET process 4G11/2 (Er)+2F7/2 (Yb)→4F9/2 (Er)+2F5/2 (Yb) is depicted in the right part of the figure. For simplicity part of the Er^{3+} energy levels are not shown or not labeled.

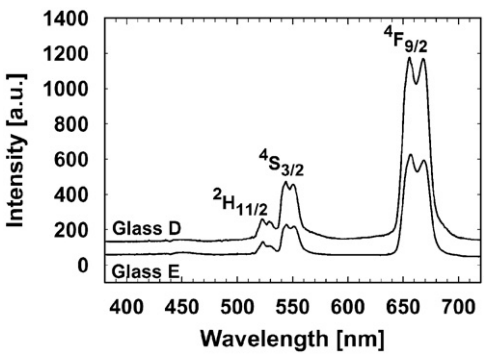

Fig. 8. Upconversion luminescence spectra of glasses D and E, excited at 940 nm.

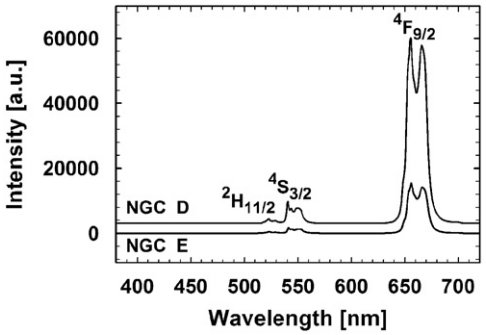

Fig. 9. Upconversion luminescence spectra of glasses D and E annealed at 693 K for 32 h and excited at 940 nm.

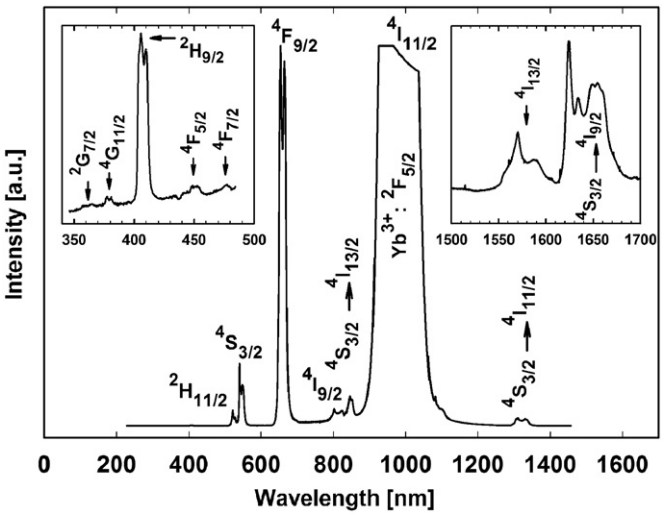

Fig. 10. Luminescence spectra of glass B annealed at 693 K for 32 h and excited at 940 nm.

3.2.3. *Anti-Stokes luminescence*

The Anti-Stokes (upconversion) luminescence spectra of glasses D and E are shown in Fig. 8, and the spectra of the respective NGC in Fig. 9. A detailed Stokes and Anti-Stokes luminescence spectra of NGC B, excited at 940 nm, is shown in Fig. 10.

The spectra of glasses D and E differ in their intensity only. The luminescence intensity of glass D is twice as high as that of glass E, which correlates with the Er^{3+} concentration in the respective glasses (see Table 1). The ratio between the intensities of red ($^4F_{9/2}$) and green ($^2H_{11/2}$ and $^4S_{3/2}$) upconversion lines is $R_{r/g} \approx 3$ and equal within the limits of error for both glasses D and E. The observed high $R_{r/g}$ values can be related to an energy cross relaxation (ECR) process between two neighboring Er^{3+} ions that populates the $^4F_{9/2}$ level bypassing the $^2H_{11/2}$ and $^4S_{3/2}$ levels and, thus, increasing the $R_{r/g}$ ratio [27,28,30,31].

The $R_{r/g}$ ratio as well as the overall luminescence intensity increases additionally in the case of high level Yb^{3+} co-doping and 940–980 nm pump [1,28,29,32]. Here, a resonant and, therefore, very efficient ET process $^4I_{15/2}$ (Er)+$^2F_{5/2}$ (Yb)→$^4I_{11/2}$ (Er)+$^2F_{7/2}$ (Yb) populates the $^4I_{11/2}$ state. A consecutive energy transfer upconversion (ETU) process $^4I_{11/2}$ (Er)+$^2F_{5/2}$ (Yb)→$^4F_{7/2}$ (Er)+$^2F_{7/2}$ (Yb) populates the $^4F_{7/2}$ level and causes intensive green and red upconversion luminescence [1,28,29,32].

In our glasses and NGC the energies of the $^4I_{11/2}$ and $^4F_{7/2}$ states are 10,000–10,500 and 20,400 cm^{-1}, respectively. The energy of the $^4F_{9/2}$ level is 15,200 cm^{-1}. So, the $^4F_{7/2}$+$^4I_{11/2}$→$^4F_{9/2}$+$^4F_{9/2}$ ECR process, proposed from Vetrone et. al. [31] is resonant. Therefore, we

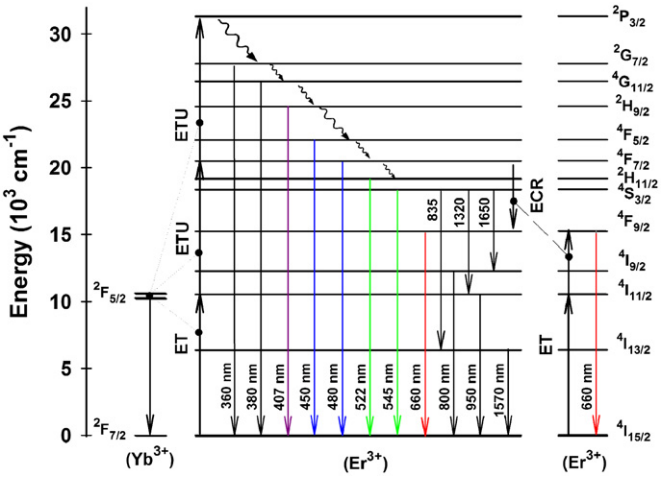

Fig. 11. Energy levels of Er^{3+} and Yb^{3+} in the glasses and glass-ceramics studied and respective pumping, and luminescence transitions under 940 nm excitation. For simplicity part of the Er^{3+} energy levels are not shown or not labeled.

suppose that this ECR process together with the ET processes discussed above (which populate efficiently the $^4I_{11/2}$ and $^4F_{7/2}$ levels) are responsible for the observed high $R_{r/g}$ ratios. This process is illustrated in the right part of Fig. 11.

An efficient ECR process, however, requires relatively short distances between the interacting Er^{3+} ions. Such distances are more natural for the NGC where, as discussed in the previous section, the rare-earth ions are concentrated. In glasses, however, with an Er_2O_3 concentration of only 0.1% and 0.2% such short distances are not possible if the Er^{3+} ions are statistically distributed. Thus, the value $R_{r/g} \approx 3$ measured in glasses can be explained only if a high degree of clustering of these ions is presumed. Moreover, the equal $R_{r/g}$ values suggest that in both glass compositions similar Er^{3+} rich clusters occur.

The upconversion luminescence in NGC is one- to two order of magnitude more intense than the luminescence in the precursor glasses. For samples with the compositions D and E this is illustrated in Figs. 8 and 9. According to Wang and Ohwaki [2] this enhancement is due to the more ordered and low phonon fluorine environment of the rare earth ions in the crystallized glasses. Actually, as discussed above, the rare earth ions are clustered into fluorine-rich regions also in the precursor glass. These regions, however, possess sub-nanometer dimensions and their luminescence is considerably affected by the oxide matrix. This influence is much smaller in the NGC. Furthermore, the higher local concentration of Yb^{3+} and Er^{3+} ions in the NGC favors the ET between them and also enhances the upconversion. Consequently, in our NGC the $^2H_{9/2}$ level of Er^{3+} ion is populated as a result of three consecutive ET upconversion steps. This is evidenced by the luminescence at 407 nm from the $^2H_{9/2}$ level, shown in Fig. 10, and is illustrated in Fig. 11. An upconversion luminescence from the $^2H_{9/2}$ level in Er/Yb co-doped oxyfluoride NGC is reported in Refs. [33,34]. There are three possible ways to populate the $^2H_{9/2}$ level of Er^{3+} due to ET processes: (1) $^4F_{7/2}$ (Er)+$^2F_{5/2}$ (Yb)→$^2P_{3/2}$ (Er)+$^2F_{7/2}$ (Yb); (2) $^4S_{3/2}$ (Er)+$^2F_{5/2}$ (Yb)→$^2G_{7/2}$ (Er)+$^2F_{7/2}$ (Yb); and (3) $^4F_{9/2}$ (Er)+$^2F_{5/2}$ (Yb)→$^2H_{9/2}$ (Er)+$^2F_{7/2}$ (Yb). In our glasses and NGCs the ET process (1), depicted in Fig. 11, is resonant. The processes (2) and (3) are not resonant and, therefore, should be phonon-assisted. They, however, are starting from the levels $^4S_{3/2}$ and $^4F_{9/2}$ which (possibly) are more populated than the $^4F_{7/2}$ level. At that point it is difficult to decide which of the processes is active in our samples.

The NGC D and E (Fig. 9) as well as the NGC B (Fig. 10) have different erbium and ytterbium concentrations but possess similar values of $R_{r/g}$ (≈ 10). This supports the presumption made in Section 3.1.2 that the phase $Pb_4Yb_3F_{17}$ doped with Er^{3+} precipitates in all studied glasses.

Fig. 11 shows the energy diagrams of Er^{3+} and Yb^{3+} ions in the respective NGC as well as the different transitions taking place under 940 nm excitation. The luminescence lines at about 835 and 1650 nm are assigned to the transitions $^4S_{3/2} \rightarrow {}^4I_{13/2}$ and $^4S_{3/2} \rightarrow {}^4I_{9/2}$, respectively, in agreement with the results of Sardar et al. [26]. Pollnau et al. [35] observed lasing at 1720 nm on the $^4S_{3/2} \rightarrow {}^4I_{9/2}$ transition in an Er^{3+} doped fluorozirconate glass fiber. The line at about 1320 nm can be assigned to the $^4S_{3/2} \rightarrow {}^4I_{11/2}$ transition if the energy of upper $^4I_{11/2}$ sublevel is presumed to be as high as 10,700 cm^{-1}. Unfortunately, the transitions to/from the $^2F_{5/2}$ (Yb^{3+}) state superimpose the transitions to/from the $^4I_{11/2}$ (Er^{3+}) state in both absorption and luminescence spectra (Figs. 5 and 10). Therefore, it is difficult to locate the exact energies of the $^4I_{11/2}$ sublevels. Additional experiments, e.g. with Ytterbium free NGC, are required to prove this hypothesis.

4. Conclusions

Homogeneous oxyfluoride glasses were prepared in the system SiO_2–B_2O_3–PbO–CdO–PbF_2–CdF_2–YbF_3–ErF_3 if the melting temperature is kept below 1173 K. Probably, clusters enriched in erbium, ytterbium and fluorine with almost constant composition are formed in the glasses. The rare earth elements facilitate nucleation and crystallization. Transparent nano glass-ceramics were obtained by annealing the glasses at temperatures in the range from 683 to 703 K for 3–30 h. The thermal properties and the crystallization kinetics are consistent with the model of kinetically self-constrained crystallization. Erbium-doped nano crystallites with the composition $Pb_4Yb_3F_{17}$ are precipitated in the glasses studied. The luminescence behavior of glasses and nano glass-ceramics are consistent with the presumed structural peculiarities.

References

[1] F. Auzel, Chem. Rev. 104 (2004) 139–173.
[2] Y. Wang, J. Ohwaki, Appl. Phys. Lett. 63 (1993) 3268–3270.
[3] P.A. Tick, N.F. Borelli, L.K. Cornelius, M.A. Newhouse, J. Appl. Phys. 78 (1995) 6367–6374.
[4] J. Qiu, Y. Kawamoto, J. Zhang, J. Appl. Phys. 92 (2002) 5163–5168.
[5] G. Dantelle, M. Mortier, D. Vivien, G. Patriarche, J. Mater. Res. 20 (2005) 472–481.
[6] C. Liu, J.W. Hong, J. Heo, J. Non-Cryst. Solids 351 (2005) 2317–2323.
[7] M.A.P. Silva, Y. Messaddeq, V. Briois, M. Poulainc, S.J.L.J. Ribeiro, Braz. Chem. Soc. 13 (2002) 200–206.
[8] L.L. Kukkonen, I.M. Reaney, D. Furniss, M.G. Pellatt, A.B. Seddon, J. Non-Cryst. Solids 290 (2001) 25–31.
[9] C. Rüssel, Chem. Mater. 17 (2005) 5843–5847.
[10] R.S. Quimby, P.A. Tick, N.F. Borrelli, L.K. Cornelius, J. Appl. Phys. 83 (1998) 1649–1653.
[11] S. Haas, A. Hoell, R. Wurth, C. Rüssel, P. Boesecke, U. Vainio, Phys. Rev. B 81 (2010) 184207.
[12] A. Dib, S. Aleonard, M.T. Roux, J. Solid State Chem. 52 (1984) 292–301.
[13] A.K. Tyagi, S.J. Patwe, S.N. Achary, M.B. Mallia, J. Solid State Chem. 177 (2004) 1746–1757.
[14] J.M. Reau, P.P. Fedorov, L. Rabardel, S.F. Mater, P. Hagenmuller, Mater. Res. Bull. 18 (1983) 1235–1246.
[15] M. Mortier, P. Goldner, C. Chateau, M. Genotelle, J. Alloys Compd. 323 (2001) 245–249.
[16] M. Beggiora, I.M. Reaney, M.S. Islam, Appl. Phys. Lett. 83 (2003) 467–469.
[17] S. Woltz, C. Rüssel, J. Non-Cryst. Solids 337 (2004) 226–231.
[18] R.P.F. de Almeida, C. Bocker, C. Rüssel, Chem. Mater. 20 (2008) 5916–5921.
[19] C. Bocker, C. Rüssel, J. Eur. Ceram. Soc. 29 (2009) 1221–1225.
[20] C. Bocker, S. Bhattacharya, T. Höche, C. Rüssel, Acta Mater. 57 (2009) 5956–5963.
[21] C. Bocker, I. Avramov, C. Rüssel, Scr. Mater. 62 (2010) 814–817.
[22] R. Wurth, F. Munoz, M. Müller, C. Rüssel, Mater. Chem. Phys. 116 (2009) 433–437.
[23] S. Bhattacharya, C. Bocker, T. Heil, J.R. Jinschek, T. Höche, C. Rüssel, H. Kohl, Nano Lett. 9 (2009) 2493–2496.
[24] N. Tsakiris, P. Agyrakis, I. Avramov, C. Bocker, C. Rüssel, Eur. Phys. Lett. 89 (2010) 18004.
[25] I. Avramov, C. Rüssel, N. Kolkovska, I. Georgiev, J. Phys.: Condens. Matter 20 (2008) 335203.
[26] D.K. Sardar, J.B. Gruber, B. Zandi, J.A. Hutchinson, C.W. Trussell, J. Appl. Phys. 93 (2003) 2041–2046.
[27] M. Takahashi, M. Izuki, R. Kanno, Y. Kawamoto, J. Appl. Phys. 83 (1998) 3920–3922.
[28] A. Patra, Ch.S. Friend, R. Kapoor, P.N. Prasad, J. Phys. Chem. B 106 (2002) 1909–1912.
[29] F. Vetrone, J.-C. Boyer, J.A. Capobianco, A. Speghini, M. Bettinelli, J. Phys. Chem. B 107 (2003) 1107–1112.
[30] J.-L. Adam, Chem. Rev. 102 (2002) 2461–2476.
[31] F. Vetrone, J.-C. Boyer, J.A. Capobianco, A. Speghini, M. Bettinelli, Chem. Mater. 15 (2003) 2737–2743.
[32] H. Sun, L. Zhang, J. Zhang, L. Wen, C. Yu, S. Dai, L. Hu, Z. Jiang, Solid State Commun. 133 (2005) 781–784.
[33] X. Qiao, X. Fan, M. Wang, J.-L. Adam, X. Zhang, J. Phys.: Condens. Matter 18 (2006) 6937–6951.
[34] J. del-Castillo, A.C. Yanes, J. Méndez-Ramos, V.K. Tikhomirov, V.D. Rodríguez, Opt. Mater. 32 (2009) 104–107.
[35] M. Pollnau, Ch. Ghisler, G. Bunea, M. Bunea, W. Lüthy, H.P. Weber, Appl. Phys. Lett. 66 (1995) 3564–3566.